ENGINEERING Information Technology & Electronic Engineering
https://www.academax.com/EITEE; https://www.engineering.org.cn
https://ieeexplore.ieee.org/xpl/RecentIssue.jsp?punumber=11344065
E-mail: eng.itee@zju.edu.cn

Engineering Journals
Available on IEEE Xplore®

Research Article
https://doi.org/10.1631/ENG.ITEE.2026.0100

A measurement-oriented magnetic pose tracking framework for biaxial rotating permanent-magnet systems

Taili WANG[1], Zhidong WU[1]✉, Bin YANG[1], Liangwei YANG[1], Ding WANG[1], Zheng LIU[1], Chengrun WU[2]

[1]*School of Information System Engineering, Information Engineering University, Zhengzhou 450001, China*
[2]*School of Medical Technology, Beijing Institute of Technology, Beijing 100081, China*

Abstract: High-precision magnetic positioning has been widely used in surgical navigation, capsule endoscopy, and other medical engineering applications, and has become an important topic in the Internet of Things. According to the magnetic source, localization systems can be classified into alternating-current coil-based and permanent-magnet-based schemes. Owing to their compact structure, permanent-magnet-based systems are more suitable for portable and embedded applications. Compared with single-rotating permanent magnets, biaxial rotating permanent magnets provide richer magnetic field information and greater potential for six-degree-of-freedom pose tracking. However, accurate estimation in such systems remains difficult because of the nonlinear magnetic field model, symmetry-induced ambiguity, initialization sensitivity, and time-varying measurement uncertainty. To address these issues, this paper develops a measurement-oriented framework for biaxial rotating permanent-magnet pose tracking, including an observability-enhanced excitation scheme, a physically consistent initialization strategy, and an adaptive recursive reconstruction method based on trust-region optimization and residual-corrected unscented Kalman filtering. The proposed method is validated through Monte Carlo simulations, COMSOL-based finite-element analysis, and prototype experiments. The results demonstrate improved convergence reliability, reduced sensitivity to initialization and environmental uncertainty, and better repeatability and robustness in complex tracking scenarios.

Key words: Magnetic localization; Kalman filter; Biaxial rotating permanent magnets; Trust-region optimization; Internet of Things

unedited

1 Introduction

Accurate six-degree-of-freedom (6-DOF) pose tracking is essential in modern medical engineering and Internet of Things (IoT) applications, including surgical navigation systems (Sorriento et al., 2020), capsule endoscopy (Cao et al., 2025), indoor service robots (Yu et al., 2023), and wearable health monitoring devices (Al-Fuqaha et al., 2015; Perera et al., 2015). In these scenarios, reliable operation requires not only high spatial accuracy but also stable real-time response under complex environmental conditions. Nevertheless, accurate pose estimation remains challenging when measurement signals are highly nonlinear and subject to environmental disturbances and system uncertainty. High-precision localization is indispensable for contactless sensing in ambient assisted living systems (Barsocchi et al., 2013; Palopoli et al., 2015), where both safety and reliability are critical requirements.

Among existing localization technologies, magnetic field-based methods are particularly attractive because they do not require line-of-sight, can penetrate non-ferromagnetic materials, and rely on relatively simple infrastructure (Raab et al., 1979). These properties make magnetic localization suitable for enclosed, cluttered, and visually occluded environments where optical, radio-frequency, or inertial methods may suffer from visibility constraints, multipath effects, or cumulative drift (Bi et al., 2020; Yi et al., 2022; Gu et al., 2023). In addition, magnetic measurement has the potential to support compact and contactless 6-DOF sensing, which is highly desirable in portable medical and embedded IoT systems. The growing demand for indoor and healthcare positioning technologies has further driven research into magnetic field-based solutions that offer improved robustness and reduced infrastructure dependence (Barsocchi et al., 2013).

Magnetic localization systems can generally be divided into alternating-current coil-based and permanent-magnet-based schemes. Compared with coil-based systems, permanent-magnet-based systems are more compact and energy-efficient, rendering them ideal for portable and embedded implementations (Hehn et al., 2019; Popek et al., 2017). In recent years, rotating permanent magnets have attracted in-

✉Zhidong WU, 3092004009wzd@163.com
Taili WANG, https://orcid.org/0009-0006-2743-728X
Zhidong WU, https://orcid.org/0009-0003-3207-4426
Bin YANG, https://orcid.org/0000-0001-7628-5303
Liangwei YANG, https://orcid.org/0009-0000-8615-8623
Ding WANG, https://orcid.org/0000-0001-6533-9206
Zheng LIU, https://orcid.org/0000-0003-2214-717X
Chengrun WU, https://orcid.org/0009-0002-6042-4588
CLC number: TP212

Received: Apr. 20, 2026; Revision accepted: Sept. 27, 2026;
Crosschecked: Nov. 2, 2026

© The Authors 2026. Published by Zhejiang University Press Co., Ltd.
This is an open access article distributed under the terms of the CC BY-NC-ND license (https://creativecommons.org/licenses/by-nc-nd/4.0/)

creasing attention because time-varying magnetic excitation can provide richer observation information than static magnetic sources. In particular, dual-rotating configurations, such as biaxial orthogonal rotating permanent magnets, offer enhanced excitation diversity and improved geometric constraints for simultaneous position-and-attitude estimation (Dong et al., 2024). Compared with single-rotating structures, they provide greater potential for improving observability and mitigating symmetry-related ambiguity, but they also introduce stronger model nonlinearity and higher demands on state reconstruction. Recent advances in compact 6-DoF pose tracking using magnetic-inertial sensor fusion have further demonstrated the potential of rotating magnetic configurations (Dong et al., 2024).

Despite these advantages, the main challenge in biaxial rotating permanent-magnet pose tracking is not limited to estimator accuracy alone. First, the observability of the coupled position-attitude states under dual-rotating excitation has not been sufficiently analyzed. Second, the consistency between the analytical magnetic field model and the physical field distribution is often insufficiently discussed, although such consistency directly affects the validity of model-based reconstruction (Qian et al., 2025). Third, existing studies usually focus on estimation error metrics, while uncertainty-aware evaluation of measurement performance, including sensitivity to initialization, disturbance, and repeated trials, remains limited. Fourth, position and orientation estimation uncertainty analysis for magnetic localization systems is still lacking systematic evaluation frameworks (Lahdo et al., 2019). As a result, the relationship among excitation configuration, field modeling, recursive estimation, and achievable measurement reliability is still not fully established.

Existing estimation methods for magnetic localization mainly include iterative filtering and Kalman-type recursive filtering approaches. The iterated extended Kalman filter (IEKF) improves local linearization through repeated updates, but its performance still depends strongly on the quality of the initial estimate and may degrade in strongly nonlinear magnetic observation models (Lv et al., 2024). Sigma-point filtering methods, such as the scaled or augmented unscented Kalman filter variants represented here by AST-UKF and SR-UKF, can better propagate nonlinear state statistics, yet they generally rely on preset noise assumptions and remain sensitive to initialization errors, model mismatch, and abnormal observations. Adaptive residual-based methods, such as AR-UKF, improve robustness by adjusting covariance online according to innovation or residual information; however, without a physically consistent initialization mechanism, their convergence may still be unreliable when the initial state is poor or when symmetry-induced ambiguity exists (Lu et al., 2018; Li et al., 2024). The soft-magnet-based position estimation using approximate EKF with hybrid analytical-neural network models has emerged as a promising direction for handling model uncertainties (Wen et al., 2025). Relative to these methods, the TROAR-UKF adopted in this study further incorporates trust-region optimization into the reconstruction process, so that initialization and recursive updating are coupled in a more physically consistent manner. In other words, the AR-UKF version obtained by removing the trust-region optimization component retains residual adaptivity, but cannot adequately suppress the sensitivity to poor initialization or local inconsistency between the observation model and the actual magnetic field (Nara et al., 2006; Wen et al., 2025). Therefore, for biaxial rotating permanent-magnet systems, the remaining difficulties lie in simultaneously handling nonlinear reconstruction, initialization sensitivity, time-varying uncertainty, and symmetry-induced attitude ambiguity within a measurement-oriented framework.

From a measurement perspective, achievable performance depends on the consistency between the physical magnetic field and the observation model, the stability of excitation and sampling synchronization, the quality of initialization, and the propagation of uncertainty from sensor noise, environmental disturbance, and system configuration (Cichon et al., 2018). Emerging approaches based on data-driven neural networks, such as MobilePosenet, have demonstrated potential for calibration-free magnetic localization by bypassing explicit dipole modeling (Xie et al., 2025). Meanwhile, magneto-oscillatory localization methods have been explored for small-scale robots, where time-varying magnetic excitation provides rich information for state estimation (Fischer et al., 2024). Model learning techniques have also been applied to magnetic micro-robot tracking, enabling adaptive control in unstructured environments (Jia et al., 2024). Compressed sensing methods for magnetic flux map acquisition have been proposed to enhance localization accuracy with reduced sensor requirements (Patkar et al., 2024). In addition, rapid localization methods using super-resolution magnetic array data have shown promise for real-time multi-magnet tracking (Miao et al., 2024). Nevertheless, these data-driven and learning-based methods often require extensive training data or calibration procedures, and their robustness under measurement noise and hardware variability remains an open issue. Wearable reconfigurable magnetic tracking systems for wireless capsule robots have also been developed to address practical deployment challenges (Su et al., 2024). Therefore, in addition to improving estimation accuracy, it is essential to develop a framework that enhances model-consistent measurement, reduces sensitivity to uncertainty, and provides a more reliable basis for evaluating measurement performance in repeated trials.

To address these issues, this paper develops a measurement-oriented pose tracking framework for a biaxial orthogonal rotating permanent-magnet system. The main contributions are summarized as follows:

1. Measurement-oriented architecture and field model: A magnetic pose measurement architecture is established for the biaxial orthogonal rotating permanent-magnet system, and the corresponding analytical field model is formulated from the perspective of excitation configuration, observation structure, and pose observability.

2. Physically consistent and uncertainty-adaptive reconstruction: A physically consistent reconstruction strategy is developed by combining trust-region-based initialization with adaptive residual unscented Kalman filtering, so as to reduce sensitivity to initial-state uncertainty, improve robustness against time-varying disturbances, and enhance recursive estimation reliability.

3. Multi-level validation of measurement performance: The proposed framework is systematically validated through sensitivity and lower-bound analysis, COMSOL-based finite-element analysis, Monte Carlo simulations, and prototype experiments, thereby providing multi-level evidence for model consistency, reconstruction effectiveness, and uncertainty-related measurement performance.

unedited

In the proposed system, only a compact tri-axial sensor is attached to the tracked target while the rotating-source module remains entirely external. This external-source/small-on-target topology makes the framework directly applicable to industrial metrology and collaborative-robot tool-tip tracking, and provides a positive methodological reference for magnetic guidance in capsule-endoscopy and surgical-navigation scenarios.

The remainder of this paper is organized as follows. Section 2 introduces the system architecture and magnetic field model of the biaxial orthogonal rotating permanent-magnet system. Section 3 presents the proposed reconstruction method. Section 4 reports the simulation and experimental results and discusses measurement performance under uncertainty. Section 5 concludes the paper.

2 Physical Modeling and Observability Analysis of the Dual-rotating Permanent Magnet Measurement System

This section presents the architecture of the biaxial rotating permanent-magnet measurement system, the corresponding time-varying magnetic field model, the observability characteristics of the dual-source excitation scheme, and the major uncertainty sources affecting practical measurement performance. The purpose of this section is not only to formulate the magnetic observation equation, but also to clarify why the adopted excitation structure is physically suitable for six-degree-of-freedom (6-DOF) pose reconstruction and how its performance depends on field modeling, geometric configuration, synchronization quality, and uncertainty propagation.

2.1 Architecture of the Biaxial Rotating Magnetic Excitation System

The overall architecture of the proposed magnetic pose measurement system is illustrated in Fig. 1, which presents the measurement chain from excitation to pose output. At the left, two orthogonally arranged rotating permanent magnets serve as the active excitation source, with Magnet 1 spinning in the *XOY* plane at f_1 = 20 Hz and Magnet 2 spinning in the *XOZ* plane at f_2 = 40 Hz. The composite magnetic field produced by both sources propagates through space and is sampled by a single tri-axial TMR sensor rigidly attached to the moving target. The raw magnetic measurements are transmitted to the host side, where synchronization with the encoder-based phase reference and pose reconstruction are performed at Fs = 1250 Hz, ultimately yielding the six degrees of freedom pose estimate $[x, y, z, \alpha, \beta, \lambda]$.

The internal structure of each functional unit is detailed in Fig. 2, from which three constituent modules can be identified:

1) A magnetic excitation unit composed of two rotating permanent magnets and their motor-drive modules;

2) A magnetic sensing unit integrated into the tracked target;

3) A host-side processing unit responsible for signal acquisition, synchronization, and pose reconstruction.

Unlike conventional single-source magnetic localization systems, the present design employs two rotating permanent magnets arranged in a biaxial and spatially separated configuration. The introduction of the dual-rotating structure is not intended merely to increase magnetic field strength. More importantly, it enriches the spatiotemporal structure of the magnetic excitation and thereby improves the observability of the target pose. In a single-magnet system, the magnetic field often exhibits strong geometric symmetry, which may lead to weak sensitivity to certain state components, multi-solution ambiguity, and pronounced dependence on initialization. By contrast, when two permanent magnets rotate in different planes and generate distinguishable time-varying field components, the resulting composite magnetic field contains more independent information in both the spatial and temporal domains. This enhanced excitation diversity improves the distinguishability of different positions and attitudes and provides a more informative basis for pose reconstruction.

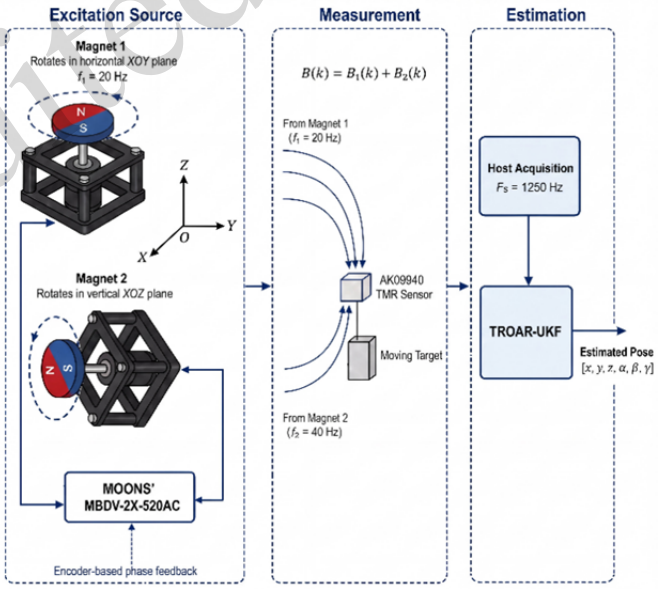


Fig. 1 Schematic of the proposed biaxial rotating permanent-magnet pose measurement system, illustrating the signal chain from dual-source magnetic excitation (Magnet 1: f_1 = 20 Hz in XOY plane; Magnet 2: f_2 = 40 Hz in XOZ plane) through tri-axial TMR sensing to host-side TROAR-UKF pose reconstruction.

Unedited

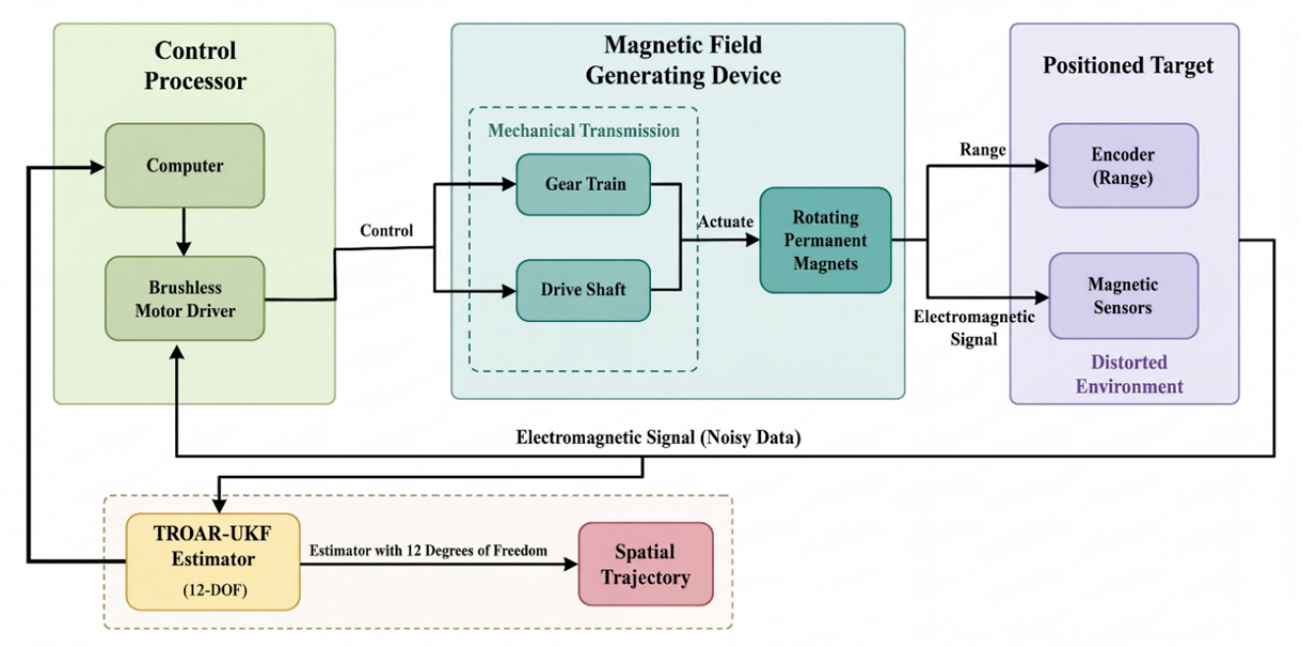


Fig. 2 Overall Architecture Design of Magnetic Field Position and Orientation Tracking System.

Cartesian coordinate system (O-XYZ) is established with the center of Magnetic Sphere 1 as the origin. The center of Magnetic Sphere 2 lies in the YOZ plane, with its axis parallel to the Y-axis and coordinates (x_0, y_0, z_0), and the sensor position at time step (k) is denoted by $p_k = [x_k, y_k, z_k]^T$. During rotation, the spatial positions of motors and magnets remain constant, while only the magnetization axis directions change dynamically. Let the rotation frequencies of Magnet 1 and Magnet 2 are f_1 and f_2 respectively, the system sampling frequency be F_s, and the initial phase angles relative to the X-axis be θ_1 (XOY plane rotation) and θ_2 (XOZ plane rotation). At the k-th sampling moment, the magnetization axis vectors of the two magnets are:

$$\mathbf{m}_1(k) = \left[\sin\left(\frac{2\pi k f_1}{F_s} + \theta_1\right), \cos\left(\frac{2\pi k f_1}{F_s} + \theta_1\right), 0 \right]^T \quad (1)$$

$$\mathbf{m}_2(k) = \left[\sin\left(\frac{2\pi k f_2}{F_s} + \theta_2\right), 0, \cos\left(\frac{2\pi k f_2}{F_s} + \theta_2\right) \right]^T \quad (2)$$

where $\mathbf{m}_1(k)=[m_1,n_1,p_1]^T$ and $\mathbf{m}_2(k)=[m_2,n_2,p_2]^T$ are unit vector of the magnetization axis. The combined alternating magnetic field at arbitrary spatial coordinates (x,y,z) is the superposition of the magnetic fields of two magnets:

$$\mathbf{B}(k,x,y,z) = \mathbf{B}_1(k,x,y,z) + \mathbf{B}_2(k,x,y,z) \quad (3)$$

where $\mathbf{B}_1$ and $\mathbf{B}_2$ are the magnetic fields generated by Magnet 1 and Magnet 2, respectively. This orthogonal excitation configuration can generate magnetic field variation patterns with distinct directional characteristics, while the dual-source structure introduces multi-directional heterogeneous time-varying excitations, which facilitates the decoupling of translational and rotational components in the measured magnetic field. Compared with a single rotating permanent magnet, the proposed biaxial rotating configuration offers three main advantages:

1. Improved observability of the 6-DOF pose state: Since the magnetic observation depends jointly on target position and sensor attitude, the introduction of a second rotating source increases the number of independent field variations and improves the sensitivity of the observation to multiple state components.
2. Suppression of symmetry-induced ambiguity: In magnetic systems with strong field symmetry, different attitudes may yield similar observations, especially when excitation diversity is limited. The dual-source rotating structure partially breaks such symmetry and reduces the probability of ambiguous pose solutions.
3. Improved robustness against local information deficiency: In some regions of the measurement space, one magnetic source may exhibit weak sensitivity to a particular state variable. The second source can compensate for this deficiency, thereby improving the spatial uniformity of the available observation information.

2.2 Time-varying Magnetic Field Model and Measurement Equation

To describe the magnetic observation process, each permanent magnet is first approximated as an equivalent magnetic dipole. Although the practical field generated by a finite-size permanent magnet deviates from that of an ideal dipole, especially in the near-field region, the dipole approximation provides an analytically tractable model and can adequately represent the magnetic field within the intended working range, as will be further examined through finite-element validation.

For the i-th permanent magnet (i=1,2), let its center be denoted by $p_{Mi} = [a_i, b_i, c_i]^T$, its equivalent dipole moment magnitude by B_T, and its unit magnetization direction at time step k by $m_i(k)$. The relative position vector from the i-th magnet to the sensor is then defined

Unedited

as $r_i(k) = p_k - p_{Mi}$. Under the magnetic dipole approximation, the magnetic flux density generated by the (i)-th rotating magnet at the sensor position can be written as:

$$\mathbf{B}_i(k) = \frac{\mu_0 m_0}{4\pi r_i^5(k)}\left(3\mathbf{r}_i(k)\mathbf{r}_i^T(k) - r_i^2(k)\mathbf{I}\right)\hat{\mathbf{m}}_i(k) \quad (4)$$

where μ_0 is the permeability of free space and I denotes the identity matrix. The total magnetic field in the global coordinate frame is obtained by the superposition of two sets of magnetic fields [see (3)].

Since the magnetic sensor is attached to the moving target, the actual measurement is represented in the sensor coordinate frame. Let the sensor attitude be described by the roll, pitch, and yaw angles $(\alpha_k, \beta_k, \gamma_k)$, and $\mathbf{R}(\alpha_k, \beta_k, \gamma_k)$ denote the corresponding rotation matrix from the global frame to the sensor frame. The magnetic observation equation is therefore given by:

$$\mathbf{Z}(k) = \mathbf{R}(\alpha_k, \beta_k, \gamma_k)\cdot\left(\mathbf{B}(k, x, y, z) + \mathbf{v}(k)\right) \quad (5)$$

where Z(k) is the observed total magnetic field signal, v(*k*) is zero-mean Gaussian white noise. The sensor attitude is described by the intrinsic Z–Y–X Euler angles $(\alpha_k, \beta_k, \gamma_k)$, where α (yaw), β (pitch), and γ (roll) denote rotations about the Z-, Y-, and X-axes respectively, and $\mathbf{R}(\alpha_k, \beta_k, \gamma_k) = \mathbf{R}_X(\gamma_k)\mathbf{R}_Y(\beta_k)\mathbf{R}_Z(\alpha_k)$ is the rotation matrix from the global frame to the sensor frame. Analysis indicates that the magnetic field value observed by the sensor varies with changes in the magnetization axis direction of the magnet, the spatial position of the sensor, and the sensor attitude. Hence, the inversion from magnetic observation to pose is intrinsically a coupled nonlinear field-to-state reconstruction problem rather than a purely kinematic state-estimation problem.

2.3 Observability Enhancement and symmetry Analysis of the Dual-rotating Configuration

For magnetic pose measurement, the reconstruction performance depends on whether the magnetic observation contains sufficient information to distinguish different state variables. The local sensitivity of the measurement to the state can be characterized by the observability matrix:

$$\mathrm{H}(x, k) = \frac{\partial h(x, k)}{\partial x} \quad (6)$$

where *h(x,k)* denotes the nonlinear observation function. The Jacobian provides a local linear description of the inverse problem around a given operating point. If a small change in a state variable produces a large change in the observed field, the corresponding state is locally sensitive and easier to identify. Conversely, if the observation changes only weakly with respect to certain state perturbations, the local reconstruction will be ill-conditioned and more susceptible to noise.

In the present system, the sensitivity is expected to vary significantly across space. Near regions where the two rotating dipole fields provide distinct directional and temporal signatures, the Jacobian norm becomes larger and the state is better conditioned. In contrast, along geometrically symmetric regions or far-field areas where the field gradient weakens, the local sensitivity decreases. This explains why the same estimator may exhibit stable convergence in some regions but slower convergence or larger variability in others. We further analyze the condition number of the observation Jacobian matrix H, the condition number κ(H) represents the sensitivity to measurement errors:

$$\kappa(\mathrm{H}) = \frac{\sigma_{\max}(\mathrm{H})}{\sigma_{\min}(\mathrm{H})} \quad (7)$$

where $\sigma_{\max}(\mathrm{H})$ and $\sigma_{\min}(\mathrm{H})$ are the maximum and minimum singular values of the matrix, respectively. A lower condition number indicates better estimation conditioning. Numerical analysis reveals significant differences in condition numbers across different magnetic configurations. In practice, the condition number reported in Table 1 is computed by stacking the observation Jacobian over a complete excitation period. Specifically, let $T = \mathrm{lcm}(1/f_1, 1/f_2)$ denote the fundamental period of the composite magnetic field. The stacked Jacobian is formed as:

$$\mathbf{H}_{\text{stacked}} = \begin{bmatrix} \mathbf{H}(\mathrm{x}, t_1) \\ \mathbf{H}(\mathrm{x}, t_2) \\ \vdots \\ \mathbf{H}(\mathrm{x}, t_N) \end{bmatrix} \quad (8)$$

where $t_1, t_2, \ldots, t_N$ are uniformly sampled time instants within one period *T*, and $N = T \cdot F_s$. The singular value decomposition (SVD) is then applied to $\mathbf{H}_{\text{stacked}}$:

$$\mathbf{H}_{\text{stacked}} = \mathbf{U}\mathbf{\Sigma}\mathbf{V}^T \quad (9)$$

and the condition number is obtained as $\kappa = \sigma_{\max} / \sigma_{\min}$, where $\sigma_{\max}$ and $\sigma_{\min}$ are the largest and smallest singular values on the diagonal of $\mathbf{\Sigma}$. For the biaxial rotating configuration with $f_1 = 20\mathrm{Hz}$ and $f_2 = 40\mathrm{Hz}$, the period-averaged condition number is significantly lower than that of a single rotating magnet, as shown in Table 1.

Table 1 Pose condition number under different magnet configurations

Configuration	Position κ	Attitude κ
Single rotating magnet	15.3	42.7
Biaxial rotating magnets	4.2	8.9

To contextualize the observability improvement of the biaxial configuration, we compare it with a representative single rotating-magnet system from the literature. Popek and Abbott (2017) achieved six-degree-of-freedom localization with a single rotating permanent magnet and reported millimeter-level position accuracy under controlled conditions. However, because the temporal variation is confined to a single rotation plane, such systems typically suffer from higher condition numbers in certain pose configurations. As shown in Table 1, a single rotating magnet yields κ ≈ 15.3 for position and κ ≈

unedited

42.7 for attitude in our simulation geometry. The biaxial configuration addresses this limitation by introducing a second magnet rotating orthogonally at a different frequency, thereby enriching the spatiotemporal diversity of the composite field. This architectural change reduces the condition number to 4.2 for position and 8.9 for attitude, indicating substantially improved measurement conditioning across the full six-degree-of-freedom state space.

3 Physically Consistent State Reconstruction under Initialization and Uncertainty

3.1 Reconstruction Objective and Design Logic

The analyses in Section 2 demonstrate that the biaxial rotating permanent-magnet configuration provides enhanced information richness compared to conventional single-magnet systems. The condition number of the observation Jacobian decreases from 15.3 to 4.2 for position estimation and from 42.7 to 8.9 for attitude estimation when employing dual orthogonal rotating magnets. However, this improved observability alone does not guarantee reliable state reconstruction in practical applications. Several challenges inherent to magnetic measurement systems must be addressed, including initialization sensitivity, spatially varying observability, time-varying uncertainty and attitude ambiguity.

In response to the aforementioned challenges, the estimator proposed in this paper is not merely an isolated filtering improvement algorithm, but rather a reconstruction framework specifically tailored to the measurement characteristics of the dual-axis rotating permanent magnet system. The complete workflow, as illustrated in Fig.3, comprises three main stages: initialization, prediction, and correction.

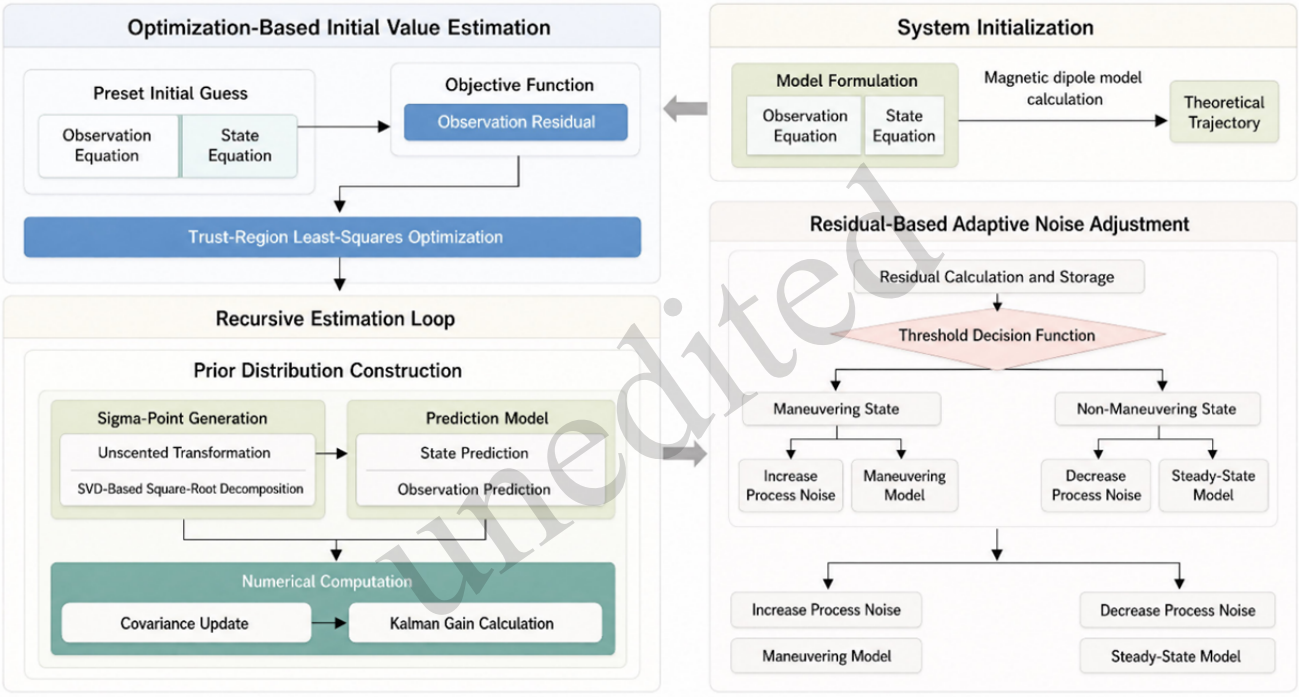


Fig. 3 Flow Chart of the Optimized Adaptive Residual-Based Unscented Kalman Filter (UKF) Algorithm.

3.2 Reconstruction Objective and Design Logic

Different from the general Unscented Kalman Filter (UKF), the proposed adaptive residual-based UKF is designed to address the inherent nonlinearities in magnetic positioning. The state equation of this algorithm is derived from target kinematics, and its parameters are updated using maneuvering and steady-state state equations according to the current motion state, ensuring physical consistency. To suppress trajectory divergence during target maneuvers, the algorithm dynamically adjusts residuals, preventing over-reliance on predictions or measurements. The state and observation equations are given as:

$$\mathbf{z}_{k_s}=\begin{pmatrix} po\mathbf{S}_k \\ \boldsymbol{\theta}_k \\ \boldsymbol{v}_k \\ \boldsymbol{\omega}_k \end{pmatrix}=\begin{pmatrix} po\mathbf{S}_{k-1} \\ \boldsymbol{\theta}_{k-1} \\ \boldsymbol{v}_{k-1} \\ \boldsymbol{\omega}_{k-1} \end{pmatrix}+\begin{pmatrix} \boldsymbol{v}_{k-1} \\ \boldsymbol{\omega}_{k-1} \\ a_{k-1} \\ 0 \end{pmatrix}\Delta t+\boldsymbol{\varepsilon}_k \tag{10}$$

$$\mathbf{z}_{k_m}=\begin{pmatrix} po\mathbf{S}_k \\ \boldsymbol{\theta}_k \\ \boldsymbol{v}_k \\ \boldsymbol{\omega}_k \end{pmatrix}=\begin{pmatrix} po\mathbf{S}_{k-1} \\ \boldsymbol{\theta}_{k-1} \\ \boldsymbol{v}_{k-1} \\ \boldsymbol{\omega}_{k-1} \end{pmatrix}+\begin{pmatrix} \boldsymbol{v}_{k-1} \\ \boldsymbol{\omega}_{k-1} \\ \boldsymbol{\omega}_{k-1}\times\boldsymbol{v}_{k-1} \\ 0 \end{pmatrix}\Delta t+\boldsymbol{\varepsilon}_k \tag{11}$$

$$\mathbf{h}_k=m_0\mathbf{R}\left(\alpha_k,\beta_k,\gamma_k\right)\sum_{i=1}^{2}\left(\frac{3\left(\mathbf{M}_{i,k}\bullet\mathbf{r}_{i,k}\right)\bullet\mathbf{r}_{i,k}-\mathbf{M}_{i,k}\bullet\left|\mathbf{r}_{i,k}\right|^2}{\left|\mathbf{r}_{i,k}\right|^5}\right) \tag{12}$$

unedited

In the state equation, the state vector at time k comprises sensor coordinates $po\mathbf{S}_k$ =(x_k,y_k,z_k), attitude angles $\boldsymbol{\theta}_k$=(α_k, β_k, γ_k), linear velocities $\boldsymbol{v}_k$ =($v_{x,k}$, $v_{y,k}$, $v_{z,k}$), angular velocities $\boldsymbol{\omega}_k$ =($\omega_{x,k}$, $\omega_{y,k}$, $\omega_{z,k}$), and process noise ε_k. To accurately reconstruct dynamic trajectories, we perform differential processing on the complex motion trajectory and discretize motion paths collected by the sensor into time-step units. The motion between discrete time steps k−1and k is modelled as a circular arc with the centripetal acceleration term $\boldsymbol{\omega}_{k-1}\times\boldsymbol{v}_{k-1}$ is derived from circular motion dynamics. In the observation equation, $\mathbf{m}_0$ is the magnetic moment constant, $\mathbf{R}$ is the attitude matrix, $\mathbf{M}_{i,k}$ and $\mathbf{r}_{i,k}$ are the magnetization axis and relative position vector for magnet i, where (a_i,b_i,c_i) are the fixed coordinates of the magnets. Observation noise is modelled as zero-mean Gaussian white noise.

3.3 Prior Distribution Construction

The algorithm initializes with the state vector $\hat{\boldsymbol{x}}_0 = E[X_0]$ and its covariance matrix $\boldsymbol{P}_0 = E\left[(\boldsymbol{X}_0 - \hat{\boldsymbol{x}}_0)(\boldsymbol{X}_0 - \hat{\boldsymbol{x}}_0)^T\right]$ .A set of sigma points is generated via the Unscented Transform (UT) to approximate the system's probability distribution. These points and their associated weights are calculated as follows:

$$\begin{cases} \boldsymbol{\chi}^{(0)}{}_k = \hat{\boldsymbol{x}}_k, \\ \boldsymbol{\chi}^{(i)}{}_k = \hat{\boldsymbol{x}}_k + SVD\left(\sqrt{(n+\lambda)\boldsymbol{P}_k}\right)_i, i = 1,...,n \\ \boldsymbol{\chi}^{(i+n)}{}_k = \hat{\boldsymbol{x}}_k - SVD\left(\sqrt{(n+\lambda)\boldsymbol{P}_k}\right)_i, i = 1,...,n \end{cases} \tag{13}$$

$$\begin{cases} W_0^m = \dfrac{\lambda}{n+\lambda}, \\ W_0^c = \dfrac{\lambda}{n+\lambda} + \left(1-\alpha^2+\beta\right), \\ W_i^m = W_i^c = \dfrac{1}{2(n+\lambda)}, i = 1,...,n \end{cases} \tag{14}$$

where $\lambda = \alpha^2(n+\kappa) - n$ is the scaling parameter. The spread of sigma points is governed by α (typically 0<α<1), while β=2 is used under the Gaussian noise assumption, and κ=3−n is set for state distribution tuning. Notably, traditional UKF uses Cholesky decomposition for Sigma points generation, which fails if $\boldsymbol{P}$ is non-positive definite. Conventional solution enforces positive definiteness but distort the true state distribution, introducing positioning error.

To resolve this, we replace Cholesky decomposition with Singular Value Decomposition (SVD). Let the scaled covariance matrix be $(n+\lambda)\boldsymbol{P} = \boldsymbol{U}\Sigma\boldsymbol{V}^T$, where $U = V$ for real symmetric matrices. The square root is then obtained reliably as $\sqrt{(n+\lambda)\boldsymbol{P}} = \boldsymbol{U}\sqrt{\boldsymbol{\Sigma}}$, with $\sqrt{\boldsymbol{\Sigma}} = diag\left(\sqrt{\sigma_1},\sqrt{\sigma_2},...,\sqrt{\sigma_n}\right)$ .This SVD-based approach ensures numerical stability without introducing regularization bias, preserving the statistical integrity of the sigma points.

These sigma points are then propagated through the nonlinear state transition function:

$$\boldsymbol{\chi}_{k|k-1}^{(i)} = \mathbf{z}_k\left(\boldsymbol{\chi}_{k-1}^{(i)}\right) \tag{15}$$

$$\boldsymbol{x}_{k|k-1} = \sum_{i=0}^{2n} W_i^{(m)} \boldsymbol{\chi}_{k|k-1}^{(i)} \tag{16}$$

$$\mathbf{P}_{k|k-1} = \sum_{i=0}^{2n} W_i^{(c)} \left(\boldsymbol{\chi}_{k|k-1}^{(i)} - \boldsymbol{x}_{k|k-1}\right)\left(\boldsymbol{\chi}_{k|k-1}^{(i)} - \boldsymbol{x}_{k|k-1}\right)^T + \mathbf{Q} \tag{17}$$

where $W_i^{(m)}$ and $W_i^{(c)}$ are the weights for the mean and covariance, respectively, and $\mathbf{Q}$ is the process noise covariance matrix.

3.4 Prior Distribution Construction

First, the predicted Sigma points are transformed into the observation space via the observation model, resulting in predicted observations:

$$\mathbf{z}_{k|k-1}^{(i)} = h\left(\boldsymbol{x}_{k|k-1}^{(i)}\right) \tag{18}$$

Subsequently, the predicted observation and covariance matrices are computed as weighted sums of these mapped points:

$$\mathbf{z}_{k|k-1} = \sum_{i=0}^{2n} W_i^{(m)} \mathbf{z}_{k|k-1}^{(i)} \tag{19}$$

$$\mathbf{S}_k = \sum_{i=0}^{2n} W_i^{(c)} \left(\mathbf{z}_{k|k-1}^{(i)} - \mathbf{z}_{k|k-1}\right)\left(\mathbf{z}_{k|k-1}^{(i)} - \mathbf{z}_{k|k-1}\right)^T + \mathbf{R} \tag{20}$$

$$\mathbf{C}_k = \sum_{i=0}^{2n} W_i^{(c)} \left(\boldsymbol{\chi}_{k|k-1}^{(i)} - \boldsymbol{x}_{k|k-1}\right)\left(\mathbf{z}_{k|k-1}^{(i)} - \mathbf{z}_{k|k-1}\right)^T \tag{21}$$

where $\mathbf{S}_k$ denotes observation covariance, $\mathbf{C}_k$ is cross-covariance and $\mathbf{R}$ is observation noise covariance. The Kalman gain $\mathbf{K}_k$, innovation sequence $\boldsymbol{\nu}_k$, and updated state/covariance are then derived:

$$\mathbf{K}_k = \frac{\mathbf{C}_k}{\mathbf{S}_k} \tag{22}$$

$$\boldsymbol{\nu}_k = \boldsymbol{x}_k - \mathbf{z}_{k|k-1} \tag{23}$$

$$\boldsymbol{x}_k = \boldsymbol{x}_{k|k-1} + \mathbf{K}_k\boldsymbol{\nu}_k \tag{24}$$

$$\mathbf{P}_k = \mathbf{P}_{k|k-1} - \mathbf{K}_k\mathbf{S}_k\mathbf{K}_k^T \tag{25}$$

Here, $\boldsymbol{x}_k$=$\mathbf{B}_{measured,k}$ is the actual noisy magnetic field measurement and P_k characterizes state estimation uncertainty.

The fixed process noise covariance $\mathbf{Q}$ in standard UKF results in poor adaptability to dynamic magnetic positioning scenarios. In the initial filtering phase, state estimates are sensitive to initial values, while noise-induced errors dominate in later iterations. For maneuvering targets, a fixed $\mathbf{Q}$ fails to track rapid state changes, leading to filter divergence. This necessitates real-time adjustment of $\mathbf{Q}$ based on the target's motion state.

To address the adaptability limitation, a sliding-window residual discrimination mechanism is proposed to detect target maneuvers. The residual vector, cumulative residual, and residual positive probability are defined as:

$$\boldsymbol{\delta}_j^{(\Gamma_m)} = \boldsymbol{x}_{j,k} - \mathbf{z}_{j,k|k-1} \tag{26}$$

$$\Theta = \sum_{\tau=1}^{\Gamma_m} \boldsymbol{\delta}^{(\Gamma_m)} \tag{27}$$

unedited

$$\rho_j = \frac{1}{\Gamma_m}\sum_{\tau=1}^{\Gamma_m}\mu\left\{\delta_j^{(\Gamma_m)} > 0\right\}, j = 1,2,3 \quad (28)$$

where Γ_m is the sliding window size, $\mu\{.\}$ is used to calculate the probability that the residual part is greater than zero.

Residuals at each step are stored in a buffer to form a sequence. When full, maneuver detection starts: calculate each component's positive probability, then its offset from s (Gaussian expectation=0.5) via a statistical function.

$$\zeta = \sum_{j=1}^{3}\sqrt{\left(\delta_j^{(\Gamma_m)} - s\right)^2} \quad (29)$$

To enhance precision, the process noise for velocity and angular velocity states is attenuated. This is achieved by applying a diagonal scaling matrix **D** with elements 0<*c*<1 to **Q**:

$$\mathbf{Q}_{k+1} = \mathbf{D}_{n,n}\mathbf{Q}_k\mathbf{D}_{n,n}^T,\ \mathbf{D}_{n,n} = diag(a), a = \begin{cases}1, n = 1,...,6\\ c, n = 7,...,12\end{cases} \quad (30)$$

The noise covariance **Q** is attenuated to improve steady-state accuracy, with a constraint matrix $\mathbf{Q}_{\min}$ to prevent over-attenuation:

$$\mathbf{Q}_{k+1} = \max\left(\mathbf{Q}_{k+1}, \mathbf{Q}_{\min}\right) \quad (31)$$

To improve the filter's responsiveness and avoid tracking lag, the process noise for kinematic states is amplified using a diagonal matrix *A* with elements *d*>1:

$$\mathbf{Q}_{k+1} = \mathbf{A}_{n,n}\mathbf{Q}_k\mathbf{A}_{n,n}^T,\ \mathbf{A}_{n,n} = diag(b), b = \begin{cases}1, n = 1,...,6\\ d, n = 7,...,12\end{cases} \quad (32)$$

This increases the uncertainty in the state prediction, allowing the filter to rely more on new measurements and rapidly correct the estimate.

Magnetic field symmetry induces a π-ambiguity in attitude estimation. Reversing the magnet's magnetization direction by 180° does not alter the measured field magnitude, leading to attitude errors of π radians. To resolve this ambiguity, a continuity constraint on the magnetic field vector is applied. Define the dot product of consecutive predicted magnetic field vectors as:

$$\Lambda = \mathbf{z}_{pred}^T\mathbf{z}_{prev} \quad (33)$$

If Λ<0, it indicates a physically implausible reversal in the field direction prediction. The correction is applied by inverting the current prediction and the corresponding sigma points in the measurement space:

$$\begin{cases}\mathbf{z}_{pred} = -\mathbf{z}_{pred}\\ \mathbf{z}_{k|k-1}^{(i)} = -\mathbf{z}_{k|k-1}^{(i)}\end{cases} \quad (34)$$

This inversion corresponds to a π-rotation of the attitude angle around the Z-axis, with the implicit relationship:

$$-\mathbf{B}_{pred} = \left(-{}_B^A\mathbf{R}\right)\mathbf{B}_{total} = \left({}_B^A\mathbf{R}'\,{}_{z(\pi)}^A\mathbf{R}\right)\mathbf{B}_{total} \quad (35)$$

where ${}_{z(\pi)}^A\mathbf{R}$ is the Z-axis π-rotation matrix. This method eliminates 180° attitude jumps without complex optimization, ensuring smooth, accurate attitude estimation.

4 Validation of Measurement Performance and Reconstruction Robustness

To evaluate the proposed magnetic position-and-attitude measurement framework, a comprehensive investigation was carried out through 100-run Monte Carlo simulations, COMSOL Multiphysics-based finite-element analysis, and physical experiments. The purpose of this section is not only to assess estimation accuracy, but also to examine measurement reliability under repeated trials, sensitivity to initialization, adaptability to time-varying noise, and the influence of major uncertainty sources on overall measurement performance. The evaluation therefore considers position and attitude errors, convergence behavior, response speed, and robustness under dynamic conditions, together with repeatability-related observations obtained from repeated runs.

4.1 Calibration and Synchronization Considerations

Before each experimental run, the sensor array and the rotating magnetic sources were mechanically aligned to reduce geometric installation error, and the acquisition chain was checked to ensure consistent timing between magnetic excitation and signal sampling. This calibration and synchronization procedure is important because even small installation deviations or phase offsets may introduce systematic bias into the inverse estimation process. In the present study, synchronization consistency was maintained throughout repeated tests to reduce inter-run variability. Nevertheless, residual timing error, installation tolerance, and environmental magnetic disturbance remain contributors to the overall measurement uncertainty and therefore should be taken into account when interpreting the experimental results.

4.2 Comparative Evaluation Under Repeated Simulations

Fig. 4 presents a comparative evaluation of the proposed method against EKF, PF, AST-UKF, SR-UKF, IEKF, and AR-UKF. The results show that TROAR-UKF provides more accurate and stable state reconstruction for the considered magnetic measurement system than the other methods, indicating that the proposed physically consistent and uncertainty-adaptive strategy is better matched to the nonlinear and uncertainty-affected observation characteristics of the present problem. Compared with AR-UKF, TROAR-UKF further improves convergence behavior and reduces sensitivity to initialization by incorporating trust-region optimization into the recursive reconstruction process.

Unedited

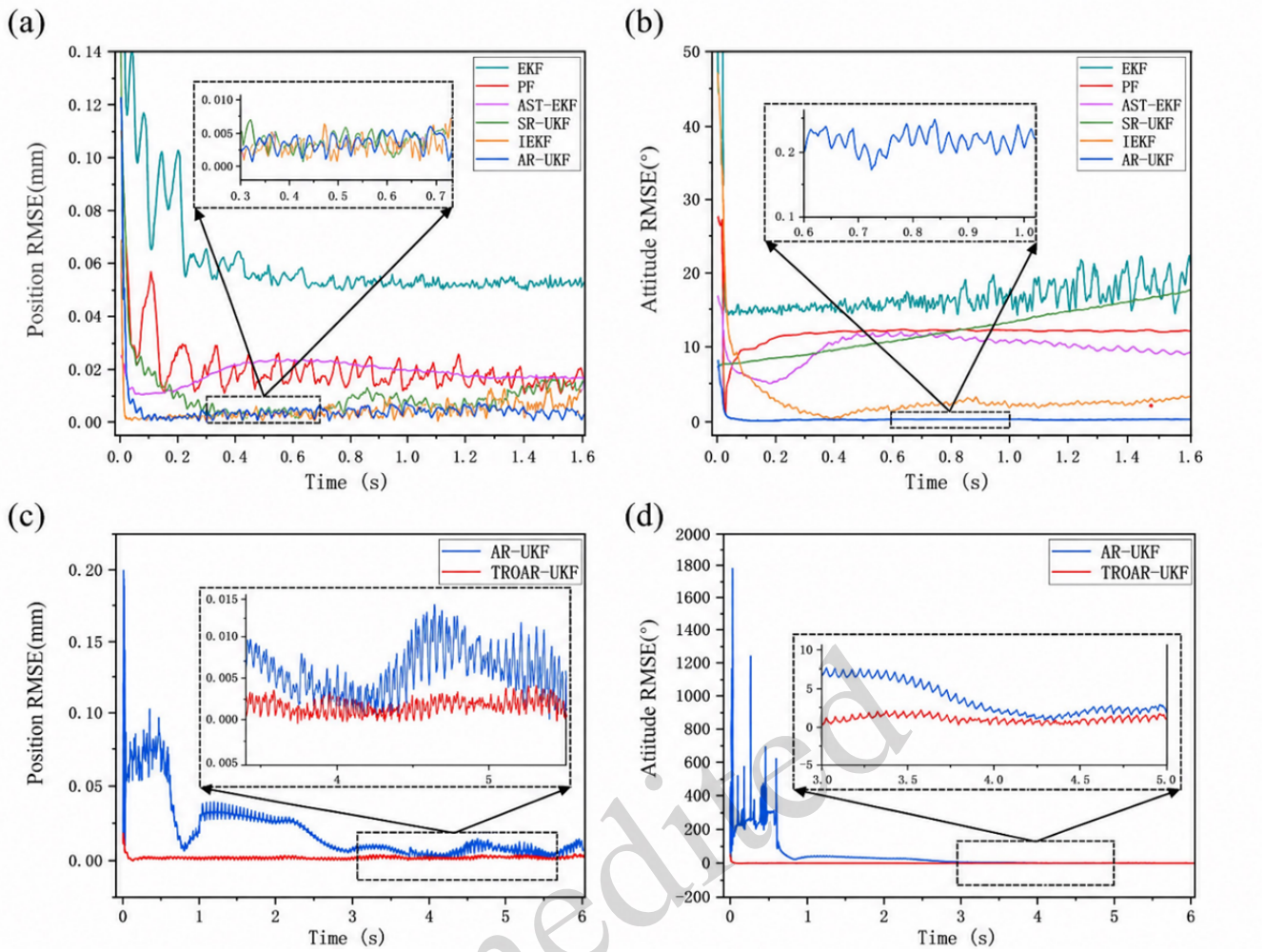


Fig. 4 Comparative evaluation of representative estimation methods for magnetic position-and-attitude measurement. (a) Position RMSE and (b) attitude RMSE for conventional methods; (c) position RMSE and (d) attitude RMSE for UKF-based methods under dynamic motion conditions.

unedited

However, the conventional UKF performs satisfactorily only under relatively simple motion conditions, whereas practical measurements often involve more complex and highly maneuvering trajectories. To assess this issue, a composite trajectory consisting of straight-line motion and spiral ascent was designed. The results in Fig. 4(c) and Fig. 4(d) show that the standard UKF becomes prone to increased deviation and occasional divergence under complex maneuvers, mainly because fixed covariance settings cannot adequately represent the time-varying uncertainty of the measurement process. By contrast, the adaptive residual UKF (AR-UKF) updates the covariance according to innovation statistics, which leads to improved tracking reliability in dynamic scenarios.

Although adaptive covariance adjustment improves dynamic performance, repeated tests under random initialization indicate that initialization uncertainty remains a major source of measurement instability. To simulate realistic operating conditions, random initial states were introduced in the Monte Carlo analysis. Statistical results show that AR-UKF diverges, on average, once every four to six runs under random initialization, suggesting that covariance adaptation alone is insufficient to ensure reproducible convergence in practical measurements.

To reduce this limitation, a trust-region optimization module is incorporated before filtering. Specifically, trust-region optimization is performed on the measured magnetic signals to estimate physically consistent initial values, thereby reducing dependence on manually assigned initial guesses. This initialization strategy significantly improves convergence reliability and reduces sensitivity to initialization uncertainty. As shown in Fig. 5, the proposed framework exhibits more stable convergence behavior than AR-UKF alone. In addition, Table 2 provides a quantitative comparison of EKF, UKF, AR-UKF, and the proposed method at an SNR of 15 dB, further confirming the improvement in measurement accuracy and repeated-run consistency.

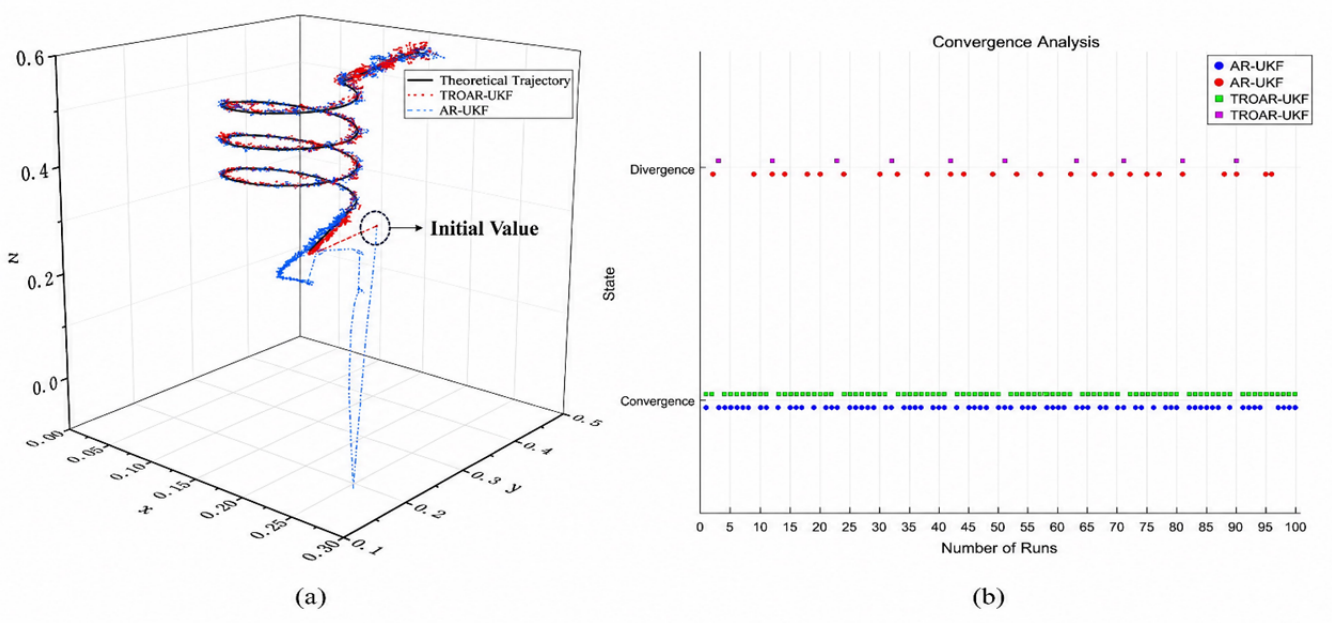


Fig. 5 Comparison of Filtering Effect and Stability between TROAR-UKF and AR-UKF.

To quantitatively evaluate and compare the tracking performance of different nonlinear filters under realistic noisy conditions, the numerical simulation results of standard EKF, PF (2000 particles, systematic resampling), AST-UKF, SR-UKF, IEKF, AR-UKF, and the proposed TROAR-UKF are summarized in Table 2. All results represent average values obtained from 100 independent Monte Carlo simulations, conducted at a signal-to-noise ratio (SNR) of 15 dB and a sampling rate of Fs=1250Hz, to account for random measurement variations and ensure statistical reliability. Position-related metrics are reported in millimeters (mm), whereas attitude-related metrics, including Euler angle errors, are reported in degrees (°).

The SNR was set to 15 dB as a deliberately conservative condition, representative of the far end of the working range and of magnetically cluttered environments; the effective SNR in the near-field core region is considerably higher. This choice ensures that the reported robustness margins are not optimistic, and the resulting trends are consistent with the physical-experiment errors in Table 3.

A simulation run is regarded as convergent only when both position and attitude errors fall below the prescribed thresholds and remain bounded throughout the observation interval: specifically, the position error is less than 50 mm, and the mean error of the three attitude angles is less than 15°, with both conditions maintained for 20 consecutive time steps. The final steady-state error, reflecting long-term tracking precision, is defined as the root-mean-square error (RMSE) achieved after convergence. The settling time denotes the time required for estimation errors to enter and remain within the predefined tolerance bounds. The convergence rate refers to the proportion of runs satisfying the convergence criterion without divergence. The run-to-run standard deviation (Run-to-run SD) represents the standard deviation of steady-state positioning error across all convergent runs, reflecting the consistency of performance across repeated trials.

Unedited

Table 2 Quantitative comparison of representative estimation methods for magnetic position-and-attitude measurement at SNR =15 dB

Method	Position RMSE (mm)	Overall Attitude RMSE (°)	Final Steady-State Error (Position/Attitude)	Computation Time Per Run/ Average Convergence Time (ms)	Average Convergence Rate (%)	Run-to-Run SD (Position/ Attitude)
EKF	54.12	14.87	45.54/12.26	21.58/9.83	35	17.85/11.02
PF (N_p=2000)	17.45	12.86	13.15/11.97	31.55/11.03	69	7.12/4.18
AST-EKF	19.31	11.85	13.71/10.22	27.32/10.51	45	16.22/9.56
SR-UKF	11.72	12.29	9.53/9.96	39.77/12.28	39	9.01/8.89
IEKF	6.55	2.74	3.64/2.25	21.39/8.54	58	4.21/2.57
AR-UKF	1.38	0.45	1.10/0.44	15.82/7.16	74	1.28/0.42
TROAR-UKF	0.97	0.38	0.84/0.35	18.21/2.73	90	0.94/0.37

4.3 Influence of key operating parameters

4.3.1 Influence of Excitation Frequency on Measurement Observability

Fig. 6(a) presents the filtering and measurement performance under different rotor speeds. As the rotation frequency of the magnetic dipoles increases, the time variation of the magnetic field becomes more pronounced, which enhances the effective field gradient and improves state observability. Under these conditions, the estimation framework responds more effectively to trajectory variation, and the measurement error decreases progressively. Increasing f_i enhances the instantaneous field variation and the effective norm of the gradient $\partial \mathbf{B}_i/\partial t$, as described by:

$$\frac{\partial B_i}{\partial t}=\frac{\partial B_i}{\partial m_i}\bullet\frac{dm_i}{dt}=\frac{\partial B_i}{\partial m_i}\bullet 2\pi f_i\begin{bmatrix}\cos\left(2\pi f_i t\right)\\ -\sin\left(2\pi f_i\right)\\ 0\end{bmatrix} \quad (36)$$

$$\left\|\frac{\partial B_i}{\partial t}\right\|\propto\left\|\frac{dm_i}{dt}\right\|\propto f_i \quad (37)$$

Furthermore, the cross-covariance $\mathbf{C}_k$ in the Kalman gain $\mathbf{K}_k=\mathbf{C}_k\mathbf{S}_k^{-1}$depends on the state sensitivity $\partial\mathbf{B}/\partial\mathbf{x}$. Thus, higher rotation speeds improve the observability, enabling the AR-UKF to respond more quickly to the dynamic changes in the trajectory and reducing the estimation delay. When the rotor frequency is lower than 15 Hz, however, the available dynamic information becomes insufficient and divergence may still occur. This behaviour indicates that excitation frequency is not merely a control parameter, but also an important measurement-design factor because it directly affects observability, sensitivity, and achievable precision. In other words, the quality of the magnetic excitation influences the amount of useful information available to the inverse estimation process. Based on the spectral characteristics of the magnetic field, the rotation-speed ratio of the two dipoles is fixed at 2:1 in the subsequent study, corresponding to 20 Hz and 40 Hz, respectively. This configuration provides sufficient spectral separation while maintaining stable operation of the measurement system.

4.3.2 Influence of Sampling Rate on Precision and Stability

To investigate the influence of the sampling rate Fs, the initial value was set to 80 Hz so as to satisfy the Nyquist criterion for the 40 Hz magnetic component. Figure 6 (b) presents the error curves obtained from 100 Monte Carlo simulations under different sampling rates. The results show that measurement accuracy improves consistently as Fs increases. This behaviour can be explained by the fact that the state transition process is intrinsically continuous, whereas the implemented estimation framework is discrete. A smaller time step Δt=1/Fs yields a closer approximation to the underlying continuous dynamics and therefore reduces discretization and truncation errors. A higher sampling rate also improves single-step prediction accuracy, particularly during rapid motion or fast magnetic rotation. From a measurement perspective, increasing the update rate provides two practical benefits. First, it enables more frequent correction of initial and transient estimation errors, which accelerates convergence. Second, it suppresses noise-induced disturbances more promptly and thereby reduces the risk of error accumulation. In addition, denser temporal sampling tends to smooth the evolution of the estimated states, which improves the numerical stability of the covariance update. These results indicate that the sampling configuration has a direct influence on both precision and real-time stability and should therefore be considered part of the measurement design rather than a purely computational parameter.

4.3.3 Influence of Residual-Based Adaptive Parameters

The influence of the residual-based adaptive parameters on measurement performance is further examined in Fig. 6(c). In particular, the sliding-window size (N) is varied while f1=20 Hz, f2=40 Hz, and Fs=1250 Hz are fixed. As (N) increases, the estimation results become smoother and the steady-state error is reduced, indicating improved attenuation of random fluctuations. At the same time, the computational latency per run also increases because maneuver detection becomes less responsive. This trade-off stems from detection delay τ_d ∝N/Fs [see (33)] and variance reduction in residual probability estimation:

$$\tau_d\propto\frac{N}{Fs} \quad (38)$$

$$Var\left(\rho_j\right)=\frac{\rho_j\left(1-\rho_j\right)}{N} \quad (39)$$

$$P_{False\ Positive}\propto\frac{\sigma_r}{\sqrt{N}} \quad (40)$$

The window length N was set to the smallest value in the low-error plateau of Fig. 6(c) that satisfies $\tau_d=N/F_s\times1000\le 40$ ms. The sensitivity of the algorithm to c and d is understood analytically: during steady motion, Eq. (29) drives $\mathbf{Q}$ to the floor $\mathbf{Q}_{\min}$ for any $c\in(0,1)$, so the steady-state RMSE is independent of the precise value of c. Upon maneuver detection, the inflation factor d (d >1) governs only the transient recovery speed; once $\mathbf{Q}$ returns to its optimal neighborhood the steady-state error is again independent of d. Consequently, any admissible pair (c, d) with 0< c <1, d >1, and $\mathbf{Q}\ge\mathbf{Q}_{\min}$ yields essentially the same steady-state accuracy, and a coarse grid search over a representative Monte Carlo subset is sufficient to fix both coefficients.

This trade-off reflects the balance between sensitivity and stability in the measurement process. A larger window provides stronger averaging and therefore improves noise suppression and repeatability under non-maneuvering conditions. However, an excessively large window prolongs the detection delay, which may lead to missed or delayed responses during rapid motion and thus degrade dynamic tracking performance. Conversely, if the threshold or window size is too small, the probability estimation becomes more sensitive to noise fluctuations, leading to false alarms and less smooth estimation curves.

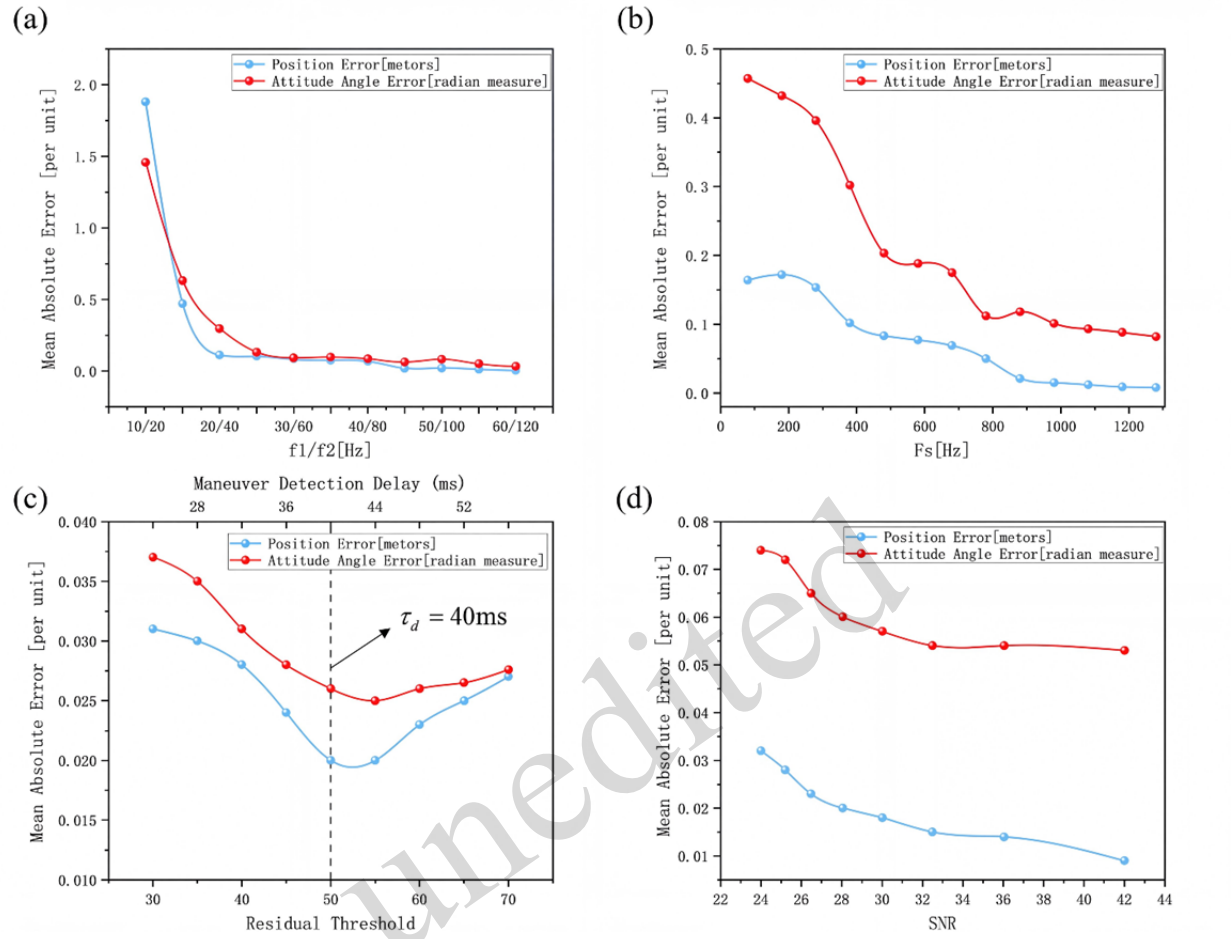
4.3.4 Influence of Noise Level and Uncertainty Adaption

Subsequently, the noise environment was varied while the remaining experimental parameters were kept unchanged, in order to assess the influence of noise power on the proposed framework. The corresponding results are shown in Fig. 6(d). The proposed method maintains relatively stable performance over a wide range of noise

Unedited

levels, indicating that the residual-adaptive mechanism can partially compensate for time-varying uncertainty and preserve reliable filtering behaviour under changing environmental conditions.

Nevertheless, the residual error still varies with the noise level, which suggests that measurement uncertainty cannot be eliminated solely by adaptive estimation. Instead, the remaining error should be interpreted as the combined result of observation noise, model mismatch, initialization quality, and dynamic operating conditions. This observation is important from a metrological perspective because it shows that the proposed framework improves robustness to uncertainty, but does not remove the need for careful system calibration and uncertainty analysis.



unedited

Fig. 6 Performance evaluation of TROAR-UKF under different parameter configurations. (a) Effect of rotor rotation frequency on estimation errors. (b) Effect of sampling frequency on estimation errors. (c) Effect of residual threshold window size *N* on estimation error and computation time. (d) Effect of measurement noise level on estimation errors.

4.4 COMSOL-Based Verification of Field-Model Consistency and Measurement-Model Validity

To validate the feasibility of the proposed magnetic field model and the associated measurement model, systematic finite-element simulations were carried out in COMSOL Multiphysics. Two N52-grade cylindrical permanent magnets were modelled with defined geometry, magnetization direction, and operating configuration, and the surrounding air domain was established to approximate the actual measurement environment. High-quality unstructured meshes were generated and checked to ensure mesh-independent field results.

The time-varying magnetic field produced by the rotating magnets was then computed under transient conditions. Uniformly distributed moving points were used to track the dynamic field variation and generate simulated trajectories, and magnetic flux density data were extracted at each sampling instant. Fig. 7. COMSOL verification of the biaxial rotating permanent-magnet field. (a)–(b) Unstructured finite-element mesh of the magnets and surrounding air domain. (c) Flux-density distribution and (d) field lines of the rotating dipoles, confirming agreement between the analytical dipole model and the computed field within the working range. These results provide a finite-element reference for examining the consistency between the analytical dipole-based field representation and the physical magnetic field in the practical operating region. The COMSOL-generated magnetic observations were subsequently used as the input to the proposed framework. The corresponding position and attitude estimation errors are shown in Fig. 8. The estimated trajectories agree well with the reference trajectories, and the attitude estimates remain bounded with relatively small fluctuation over the entire measurement interval. This result indicates that the proposed framework remains effective even when the observations are generated by a higher-fidelity physical field model rather than by the analytical model itself.

From a measurement perspective, the significance of the COMSOL analysis lies not simply in providing additional simulation sup-

port, but in verifying field-model consistency and supporting the validity of the measurement model employed in the estimator. The finite-element results indicate that the analytical dipole approximation provides an acceptable representation of the physical magnetic field within the considered measurement range, while the remaining discrepancy serves as an indicator of model-related uncertainty. This intermediate verification step is important because it links the idealized analytical formulation to the physical experimental system and helps explain the subsequent measurement performance observed in practice.

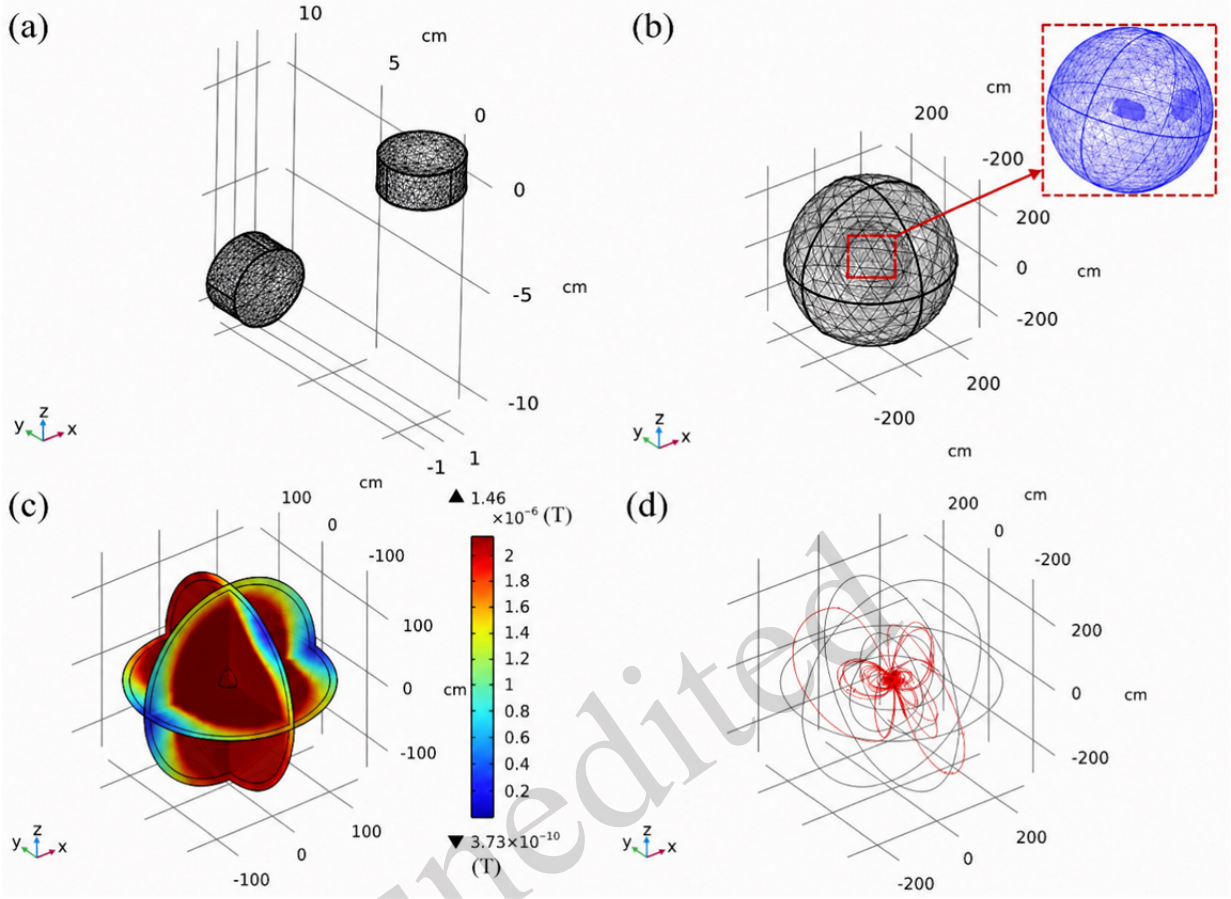


Fig. 7 (a)-(b) demonstrate the mesh generation of the permanent magnet and air domain via COMSOL; (c)-(d) show the magnetic field distribution of the magnetic dipole, including magnetic flux density and magnetic field lines.

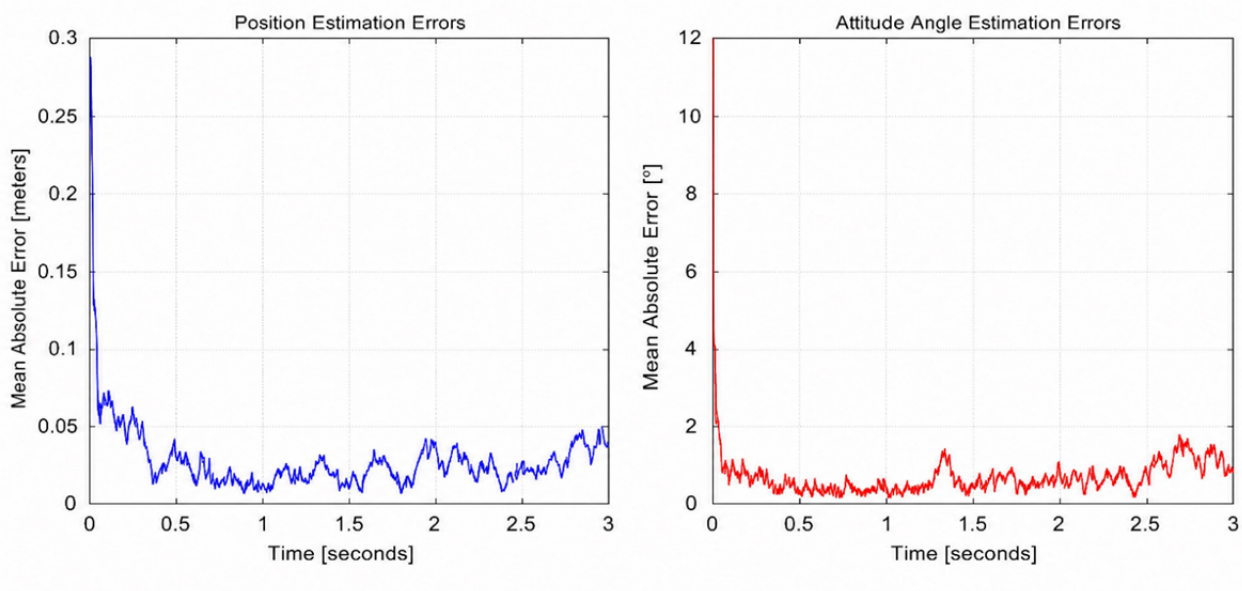


Fig. 8 Filtering results based on COMSOL solutions, where(a) and (b) show the position and attitude angle errors.

unedited

4.5 Physical experiments and practical measurement performance

Finally, physical experiments were conducted to evaluate the practical performance of the proposed magnetic position-and-attitude measurement framework. The prototype system and representative experimental scenarios are shown in Fig. 9. The experimental platform consists of the biaxial orthogonal rotating permanent-magnet excitation structure, the magnetic sensing unit, the signal acquisition and control circuit, and the host-side processing module implementing the proposed method. Detailed hardware parameters are provided in Table 4 of the Appendix.

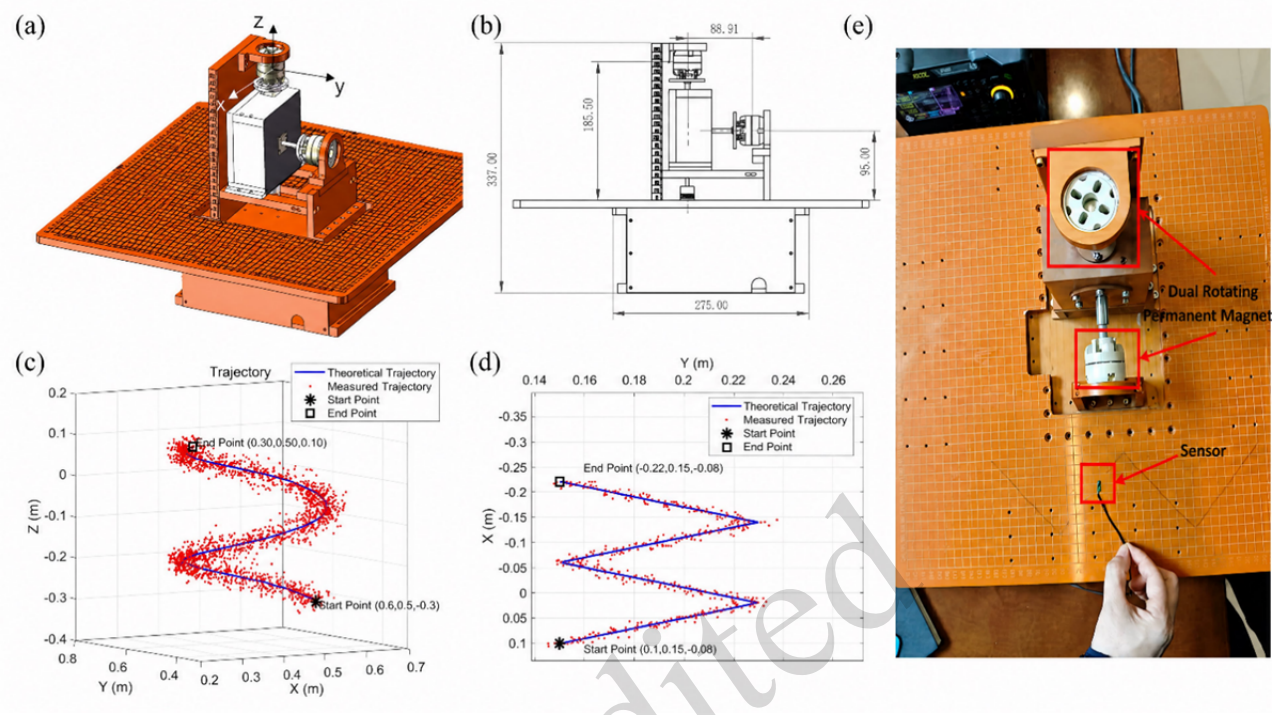


Fig. 9 Relevant images of the prototype test, where (a) and (b) are the structural diagrams of the test prototype, (c) and (d) show the estimation results of the algorithm under different trajectory conditions (spiral trajectory: 43 cm path length, 10-12 s; W-shaped trajectory: 46 cm path length, 11-13 s), and (e) is the field test demonstration.

The measurement surface was a self-healing cutting mat with a printed 1 cm grid. The sensor was placed at grid intersection points within the working range, with nominal coordinates read from the grid markings (resolution 10 mm). The spiral trajectory shown in Fig. 9(c) has a path length of approximately 43 cm and was completed in approximately 10-12 seconds, while the W-shaped trajectory in Fig. 9(d) has a path length of approximately 46 cm and was completed in approximately 11-13 seconds, corresponding to average motion speeds of approximately 35-43 mm/s and 35-42 mm/s, respectively. These timing data were obtained from the recorded timestamps of the sensor acquisition system, and the path lengths were computed by integrating the Euclidean distance between consecutive estimated positions. The moderate handheld motion speed ensures stable tracking while demonstrating the system's real-time performance under realistic manipulation conditions.

For each static test position, the sensor was held stationary for a fixed dwell interval and the mean TROAR-UKF estimate was recorded; the error was computed against the grid-defined reference. For the trajectory experiments, the start and end points were anchored to labeled grid intersections, and the theoretical path was defined by straight-line segments between those anchors. Attitude (roll γ and pitch β) was validated with a graduated rotation jig (5° steps); yaw α was not independently verified owing to field interference with any co-located heading reference. All reported static accuracy figures are given as mean ± standard deviation over repeated measurements at each grid point. The prototype provides reliable 6-DOF tracking over a sensor-to-source distance of roughly 0.24–2.15 m, with the highest accuracy in the 0.24–0.45 m core region; the near limit follows from the dipole-validity condition $r > 2R$ and the far limit from the reduced SNR under the $1/r^3$ decay. The attainable range is mildly direction-dependent owing to the asymmetric two-magnet layout.

Different motion trajectories were tested in order to assess the ability of the system to reconstruct both position and attitude in real time. In addition to the average error, attention was also paid to the consistency of the results under repeated trials, because for a measurement system, good performance should be reflected not only in nominal accuracy but also in repeatability and reproducibility.

Table 3 summarizes the performance of TROAR-UKF under two validation conditions. The COMSOL-based case reflects model-consistent finite-element observations, while the physical experiment includes additional uncertainty sources such as sensor noise, calibration deviation, synchronization error, mechanical tolerance, and environmental disturbance. Therefore, the experimental errors are expected to be larger than those in COMSOL simulation, although the overall convergence and tracking stability remain satisfactory.

unedited

Table 3 Quantitative performance indicators of TROAR-UKF under COMSOL and real-world experimental conditions.

Metric	COMSOL-based Simulation	Physical Experiment
Position RMSE (mm)	1.95	3.32
Average Attitude RMSE (°)	1.62	3.51
Mean settling time (ms)	16	27
Run-to-run SD (mm)	1.59	3.47

The experimental results show that the proposed framework achieves stable real-time trajectory tracking with millisecond-level response and millimetre-level positioning accuracy under practical operating conditions. Compared with the simulation and finite-element results, the physical experiments exhibit larger residual errors, which is expected because the practical system is affected by multiple uncertainty sources that cannot be completely eliminated in the current prototype. These sources mainly include sensor noise, deviation between the analytical magnetic model and the actual field generated by the permanent magnets, mechanical installation and alignment tolerance, rotational-speed fluctuation, and synchronization deviation between magnetic excitation and data acquisition. Environmental magnetic disturbance and structural vibration may also contribute to the residual error.

Among these factors, synchronization error deserves particular attention. Since the proposed measurement principle relies on the temporal variation of the rotating magnetic field, any phase offset between rotor motion and sensor sampling changes the effective observation sequence presented to the estimator. Such timing inconsistency directly affects the correspondence between measured and predicted magnetic signals, thereby increasing residual error and degrading consistency across repeated runs. Similarly, calibration-related deviations, such as sensor-axis misalignment, uncertainty in magnet pose, and variation in the effective magnetic moment, may introduce systematic bias into the reconstructed states. Repeated trials were conducted under the same nominal conditions to assess repeatability. The results show that the proposed framework maintains relatively small run-to-run variation in the reconstructed trajectory, indicating good repeatability of the measurement process. To assess reproducibility, additional tests under different initialization and disturbance conditions were also considered. Although the estimation error increases slightly under these more challenging conditions, the proposed method remains convergent in most runs and preserves stable overall measurement behaviour. This indicates that the trust-region initialization and residual-adaptive covariance update improve not only nominal estimation accuracy, but also the tolerance of the measurement result to practical uncertainty. Overall, the physical experiments confirm that the proposed framework is feasible for high-precision magnetic position-and-attitude measurement in practical scenarios. More importantly, the results show that the proposed method improves convergence reliability, repeatability, and robustness against uncertainty sources that are commonly encountered in real measurement systems.

5 Conclusions

This paper has presented a magnetic position-and-attitude measurement framework for a biaxial orthogonal rotating permanent-magnet system, with emphasis on both estimation accuracy and measurement reliability under practical uncertainty. To address the limitations caused by strong nonlinearity, initialization sensitivity, time-varying noise, and model-related deviations, a trust-region-optimized adaptive residual unscented Kalman filter (TROAR-UKF) was developed and integrated into the proposed framework. The method combines trust-region-based initialization, residual-adaptive covariance updating, and a dual rotating magnetic dipole configuration to improve observability, convergence reliability, and robustness. In addition to improving nominal reconstruction accuracy, these features enhance repeated-run consistency and reduce sensitivity to random initialization and changing operating conditions.

The proposed framework was validated through repeated Monte Carlo simulations, COMSOL-based finite-element analysis, and physical experiments. The results showed that TROAR-UKF outperforms AST-UKF, SR-UKF, IEKF, and AR-UKF in terms of estimation accuracy, convergence behavior, and robustness to initialization uncertainty. The COMSOL-based analysis further verified the consistency between the analytical field model and the physical magnetic field within the considered operating range, while the physical experiments demonstrated stable real-time tracking with millimetre-level positioning accuracy and millisecond-level response. Although the experimental errors were larger than those in simulation, the method maintained satisfactory convergence and relatively small run-to-run variation under practical uncertainty sources, including sensor noise, field-model mismatch, installation tolerance, synchronization deviation, and environmental disturbance.

Overall, the results indicate that the proposed TROAR-UKF-based framework is an effective approach for improving the metrological performance of magnetic position-and-attitude measurement systems. The study also shows that achievable measurement performance depends not only on the estimator itself, but also on field-model validity, excitation design, calibration quality, and synchronization stability. The present prototype is a bench-scale external platform in which only a compact sensor is attached to the tracked target; the methodology provides a positive reference for the further development of magnetic guidance systems in capsule-endoscopy and surgical-navigation scenarios, while being directly applicable to industrial metrology and collaborative-robot tool-tip tracking in its current form. Future work will focus on improving computational efficiency and exploring hybrid model-based and data-driven strategies to further enhance the real-time performance and practical applicability of magnetic measurement systems.

Unedited

Supplementary materials

Table S1 Hardware specifications of the experimental platform.

Category	Parameter	Value
TMR Sensor	Model	AK09940 (Asahi Kasei Microdevices)
	Package / footprint	11-pin LGA, 1.6 mm × 1.6 mm × 0.58 mm
	Number of sensing axes	3 (tri-axial, co-located at one point)
	Number of sensor units	1 (mounted on tracked target)
	Resolution	18 bit per axis
	Sensitivity (Low-noise drive 2, MT[1:0] = "11")	10 nT/LSB
	Full-scale range	±1200 μT per axis
	Noise floor (Low-noise drive 2)	40 nT rms
	Operating drive mode for Fs	Single Measurement, Low-power drive 1 (MT[1:0] = "00")
	Data output rate Fs	1250 Hz
	Communication interface	I²C, 400 kHz
Permanent Magnets	Grade / material	N52 sintered NdFeB
	Shape	Cylinder
	Diameter × height	34 mm × 16 mm
	Remanence B_r	1.44–1.48 T
	Coercivity H_c	995–1115 kA/m
	Equivalent dipole moment m_0	16.65–17.12 A·m²
	Quantity	2 (geometrically identical)
	Magnet 1: rotation plane / frequency	XOY plane / f_1 = 20 Hz
	Magnet 2: rotation plane / frequency	XOZ plane / f_2 = 40 Hz
Servo Drive	Model	MOONS' MBDV-2X-520AC (dual-axis)
	Input voltage	24–60 VDC
	Supply voltage used	24 V (switch-mode power supply)
	Control mode	Closed-loop velocity control
	Feedback	Incremental encoder (per axis)
	Steady-state speed ripple	< 1 % of set point
Mechanical Frame	Structural material	Phenolic resin (Bakelite)
	Magnetic interference	None (non-magnetic material)
Synchronization	Method	Encoder-based, sample-by-sample phase readout
	Phase update latency	< 1 drive control cycle (≪ 0.8 ms sampling interval)
	Phase quantities derived	Instantaneous rotor angles $\theta_1(k)$, $\theta_2(k)$ in Eqs. (1)–(2)

unedited

Acknowledgments

This work was supported by the National Natural Science Foundation of China (Nos. 22504167 and 62171469).

Author contributions

Taili WANG was responsible for the research design. The data processing was completed by Taili WANG, Zhidong WU, and Chengrun WU. The initial paper was drafted by Taili WANG, Liangwei YANG, and Zheng LIU. Bin YANG and Ding WANG helped organize the paper. The revision and finalization were accomplished by Taili WANG, Zhidong WU, Liangwei YANG, and Zheng LIU.

Conflict of interest

All the authors declare that they have no conflict of interest.

Data availability

The data that support the findings of this study are available from the corresponding author upon reasonable request.

References

Al-Fuqaha A, Guizani M, Mohammadi M, et al., 2015. Internet of Things: a survey on enabling technologies, protocols, and applications. *IEEE Commun. Surv. Tutor.*, 17(4):2347–2376. https://doi.org/10.1109/COMST.2015.2444095.

Barsocchi P, Chessa S, Furfari F, Potorti F, 2013. Evaluating ambient assisted living solutions: the localization competition. *IEEE Pervasive Comput.*, 12(4):72–79. https://doi.org/10.1109/MPRV.2013.43.

Bi JX, Wang YJ, Cao HJ, Qi HX, 2020. A method of radio map construction based on crowdsourcing and interpolation for Wi-Fi positioning system. *Proc. IEEE Int. Conf. Indoor Positioning Indoor Navig. (IPIN)*, p.1–8. https://doi.org/10.1109/IPIN.2018.8533793.

Cao Q, Pan Y, Zhang YQ, et al., 2025. A dual-functional capsule robot for drug delivery and tissue biopsy based on magnetic torsion spring technology. *J. Zhejiang Univ-Sci D*, 8(3):495–510. https://doi.org/10.1631/bdm.2400276.

Cichon D, Psiuk R, et al., 2018. A Hall-Sensor-Based Localization Method With Six Degrees of Freedom Using Unscented Kalman Filter. *IEEE Sensors Journal*, 19(7):2509-2516. https://doi.org/10.1109/TRO.2023.3303612.

Dong S, Wang H, 2024.A Compact and Robust 6-DoF Pose Tracking System Using Magnetic-Inertial Sensors and a Single Uniaxial Electromagnetic Coil. *IEEE Sensors Journal*, 24(4):5062-5072. https://doi.org/10.1109/JSEN.2023.3348243.

Fischer F, Gletter C, Jeong M, Qiu T, 2024. Magneto-oscillatory localization for small-scale robots. *npj Robotics*, 2: Article 1. https://doi.org/10.1038/s44182-024-00008-x.

Gu C, Lin W, He X, Zhang L, Zhang M, 2023. IMU-based motion capture system for rehabilitation applications: a systematic review. *Biomim. Intell. Robot.*, 3:100097. https://doi.org/10.1016/j.birob.2023.100097.

Hehn M, Sippel E, Carlowitz C, Vossiek M, 2019. High-Accuracy Localization and Calibration for 5-DoF Indoor Magnetic Positioning Systems. *IEEE Transactions on Instrumentation and Measurement*, 68(10):4135-4145. https://doi.org/10.1109/TIM.2018.2884040.

Jia YY, Miao S, Zhou JJ, et al., 2024. Efficient model learning and adaptive tracking control of magnetic micro-robots for non-contact manipulation. *Proc. IEEE Int. Conf. Robot. Autom. (ICRA)*, p.4534–4540. https://doi.org/10.48550/arXiv.2403.14414.

Lv B, Qin Y, Dai H, Han J, 2024.A Differential Signal and Extended-Kalman-Filter-Based Anti-Interference Magnetic Tracking Method for Surgical Scenes. *IEEE Transactions on Industrial Electronics*, 71(11):15140-15150. https://doi.org/10.1109/TBME.2023.3312345.

Lu ZH, Zhu MY, Ye QW, Zhou Y, 2018. Performance analysis of two EM-based measurement bias estimation processes for tracking systems. *Front. Inf. Technol. Electron. Eng.*, 19(9):1151–1165. https://doi.org/10.1631/FITEE.1800214.

Luo J, Huang Q, Dai H, Wang S, Chen Y, 2023.Adaptively Adjusted EKF-Based Magnet Tracking Method for Fast-Moving Object. *IEEE Transactions on Instrumentation and Measurement*, 72:1-9. https://doi.org/10.1109/TIM.2023.3253892.

Lahdo M, Ströhla T, Kovalev S, 2019.Design and Implementation of a New 6-DoF Magnetic Levitation Positioning System. *IEEE Transactions on Magnetics*, 55(12):1-7. https://doi.org/10.1109/TMAG.2019.2936394.

Nara T, Suzuki S, Ando S, 2006. A closed-form formula for magnetic dipole localization by measurement of its magnetic field and spatial gradients. *IEEE Trans. Magn.*, 42(10):3291–3293. https://doi.org/10.1109/TMAG.2006.879151.

Palopoli L, Argyros A, Birchbauer J, et al., 2015. Navigation assistance and guidance of older adults across complex public spaces: the DALi approach. *Intell. Serv. Robot.*, 8(2):77–92. https://doi.org/10.1007/s11370-015-0165-2.

Patkar A, Liu D, Wang Y, Youcef-Toumi K, 2024. Magnetic flux map acquisition using a compressed sensing method. *Proc. IEEE Int. Conf. Ind. Electron. Appl. (ICIEA)*, p.1–6. https://doi.org/10.1109/ICIEA61579.2024.10665180.

Perera C, Liu C, Jayawardena S, 2015. The emerging Internet of Things marketplace from an industrial perspective: a survey. *IEEE Trans. Emerg. Top. Comput.*, 3(4):585–598. https://doi.org/10.1109/TETC.2015.2396574.

Popek KM, Schmid T, Abbott JJ, 2017. Six-degree-of-freedom localization of an untethered magnetic capsule using a single rotating magnetic dipole. *IEEE Robot. Autom. Lett.*, 2(1):305–312. https://doi.org/10.1109/LRA.2016.2528265.

Qian B, et al, 2025.Magnetoquasistatic Positioning: Recent Advances, Applications, Potential Solutions, and Future Prospects. *IEEE Internet of Things Journal*, 12(6):6250-6274. https://doi.org/10.1109/JIOT.2025.3512341.

Raab FH, Blood EB, Steiner TO, Jones HR, 1979. Magnetic position and orientation tracking system. *IEEE Trans. Aerosp. Electron. Syst.*, AES-15(5):709–718. https://doi.org/10.1109/10.31093.

Sorriento A, Porfido MB, Mazzoleni S, et al., 2020. Optical and electromagnetic tracking systems for biomedical applications: a critical review on potentialities and limitations. *IEEE Rev. Biomed. Eng.*, 13:212–232. https://doi.org/10.1109/REBME.2020.2967521.

Su Y, Liu Y, Chen J, et al., 2024. A wearable, reconfigurable, and modular magnetic tracking system for wireless capsule robots. IEEE Trans. Ind. Informat., 20(12):13600–13611. https://doi.org/10.1109/TIM.2023.3253892.

Miao et al., 2024. A rapid localization method based on super-resolution magnetic array information for multiple magnetic targets. *Sensors*, 24(10):3226. https: //doi.org/10.3390/s24103226.

Su S, Yuan S, Li Z, Ma Y, Ma M, Ren H, 2024.A Wearable, Reconfigurable, and Modular Magnetic Tracking System for Wireless Capsule Robots.IEEE Transactions on Industrial Informatics, 20(12):13600-13611. https://doi.org/10.1109/TIE.2022.3198234.

Wen T, Liu S, Wang H, 2025.Soft-Magnet-Based Position Estimation Using an Approximate Extended Kalman Filter With a Hybrid Analytical-Neural Network Model. *IEEE Transactions on Instrumentation and Measurement*, 74:1-13. https://doi.org/10.1109/TMAG.2018.2849567.

Xie W, Zhang Y, Shan J, Sun H, Tan J, Cheng SS, 2025. Theoretical Data-Driven MobilePosenet: Lightweight Neural Network for Accurate Calibration-Free 5-DOF Magnet Localization. *IEEE Transactions on Instrumentation and Measurement*, 74:1-11. https://doi.org/10.48550/arXiv.2501.02809.

Yi J, Liu J, Zhang C, Lu X, 2022. Magnetic motion tracking for natural human computer interaction: a review. *IEEE Sensors J.*, 22(23):22356–22367. https://doi.org/10.1109/JSEN.2022.3215678.

Yu C, Zhang DH, Wu Z, et al., 2023. RFPose-OT: RF-based 3D human pose estimation via optimal transport theory. *Front. Inf. Technol. Electron. Eng.*, 24(10):1445–1457. https://doi.org/10.1631/FITEE.2200550.

unedited